PHYSICAL REVIEW X **15,** 021031 (2025)

Quantum-Enhanced Sensing of Axion Dark Matter with a Transmon-Based Single Microwave Photon Counter

C. Braggio,[1,2,*] L. Balembois,[3] R. Di Vora,[4] Z. Wang,[3] J. Travesedo,[3] L. Pallegoix,[3] G. Carugno,[2] A. Ortolan,[4] G. Ruoso,[4] U. Gambardella,[5] D. D'Agostino,[5] P. Bertet,[3] and E. Flurin[3,†]

[1]*Dipartimento di Fisica e Astronomia, Università di Padova, Padova, Italy*
[2]*INFN, Sezione di Padova, Padova, Italy*
[3]*Quantronics group, Université Paris-Saclay, CEA, CNRS, SPEC, 91191 Gif-sur-Yvette Cedex, France*
[4]*INFN Laboratori Nazionali di Legnaro, Legnaro, Padova, Italy*
[5]*INFN, Sezione di Napoli, Napoli, Italy*

(Received 22 May 2024; revised 6 December 2024; accepted 24 February 2025; published 28 April 2025)

We report an axion dark matter search with a haloscope equipped with a microwave photon counter. The haloscope is a tunable high quality factor three-dimensional microwave cavity placed in a magnetic field. The photon counter, operated cyclically, maps an incoming microwave photon onto the state of a superconducting transmon qubit. The measurement protocol continuously monitors the power emitted by the haloscope cavity as well as the dark count background and enables tuning of the cavity frequency to probe different axion masses. With this apparatus, we enhance by a factor of 20 the search speed that can be reached with quantum-limited linear amplifiers and set a new standard for probing the existence of axions with resonant detectors above 5 GHz.

DOI: 10.1103/PhysRevX.15.021031 Subject Areas: Cosmology, Quantum Physics

I. INTRODUCTION

The cosmological model that best complies with the astronomical observations collected over years [1] invokes the existence of dark matter (DM), having observable gravitational effects but interacting weakly with ordinary matter. For decades, experiments with increasing scale and cost have been deployed relying on the hypothetical interaction of DM with the particles of the standard model as devised in specific theoretical models. These tests have set stringent constraints to the concept of the weakly interacting massive particle [2] in the mass range 1 GeV–10 TeV [3,4]. On the ultralight side of the open parameter space, the cold-dark-matter paradigm is pursued with a radically different approach [5,6]. At this frontier of fundamental physics, diverse small-scale experiments rely on quantum sensing [7] to improve their sensitivity to new particles and forces in specific mass ranges, with a large discovery potential.

A prominent example is the cavity axion haloscope, a detector consisting of a 3D microwave resonator permeated by an intense magnetic field and readout by an heterodyne receiver [8].

The extremely weak interaction of the axion with electromagnetism is parametrized by $g_{a\gamma\gamma}$ in the Lagrangian $\mathcal{L} = g_{a\gamma\gamma} a\mathbf{E}\cdot\mathbf{B}$, where a is the axion field and $\mathbf{E}$ and $\mathbf{B}$ are, respectively, the electric and magnetic fields. This coupling allows axion to photon conversion in a static magnetic field $\mathbf{B} = B_0$ with rate scaling as B_0^2.

The cavity frequency ν_c sets the particle mass $m_a = h\nu_c$ ($10\mu\text{eV} \simeq 2.5$ GHz) at which the signal is resonantly enhanced; therefore, wide tunability is a main requirement beyond sensitivity, defined as the minimum measurable signal power in the presence of receiver noise. Plots of the $g_{a\gamma\gamma}$ versus axion mass m_a summarize the already investigated region for these two parameters describing axion-like particles (ALPs), namely, dark matter particles with the same phenomenology as the axions of quantum chromodynamics (QCD). ALPs arise in models unrelated to the strong *CP* problem, to which the QCD axion provides instead a solution [9]. Haloscope best sensitivities have been obtained in the frequency range from 600 MHz to 1 GHz where signal and noise power compare favorably. Here, superconducting quantum interference device (SQUID) technology and quantum-limited linear amplifiers have enabled probing axion-photon couplings down to 3×10^{-16} GeV^{-1} [10,11] predicted by QCD axion models. However, a large part of the parameter space is yet unexplored at higher frequencies as the scan rate decreases with the search frequency as ν_c^{-4} (see the Appendix). Even

---

[*] Contact author: caterina.braggio@unipd.it
[†] Contact author: emmanuel.flurin@cea.fr

in the most favorable conditions, assuming haloscopes equipped with the best superconducting magnets delivering fields up to 14 T and state-of-the-art superconducting cavities [12] with linewidths $\Delta\nu_c$ matching that of the axion signal $\Delta\nu_a = \nu_c/10^6$ [13], the time needed to scan the 1–10 GHz decade with relevant sensitivity can be estimated around hundreds of years if a detection chain based on the measurement of the field quadratures with a linear amplifier is employed. The limiting factor arises from the vacuum state not being an eigenstate of the quadrature operators, which causes the output standard deviation to reach at best an effective noise temperature of half a photon (effective mean occupation number $\bar{n}_{\mathrm{SQL}} = 1$); this is called the standard quantum limit (SQL).

A scheme without amplifier noise is based on a cavity-Rydberg atom system, used in the CARRACK experiment [14] to perform an axion search in the 8% mass range around 10 μeV. In superconducting circuits, microwave squeezing is a method to circumvent this fundamental noise, which has allowed for accelerating an axion search by a factor of 2 [15,16]. Here, we target a larger enhancement by using single microwave photon detectors (SMPDs) to read out the cavity signal [17]. Compared to quadrature detection at the SQL, a photon counter with dark count rate Γ_{dc} and detector efficiency η, allows for a a speed enhancement by $\mathcal{R} = \eta^2\Delta\nu_a/\Gamma_{\mathrm{dc}}$ (see the Appendix).

A lower bound for the SMPD dark count rate can be obtained by considering the mean photon number $\bar{n}_{\mathrm{th}} = 1/(e^{h\nu/k_B T} - 1)$ of an electromagnetic mode at frequency ν and temperature T. The dark count rate is then given by $\Gamma_{\mathrm{dc}} = \bar{n}_{\mathrm{th}}\eta\Delta\nu_c$. For instance, in an experiment at $T =$ 20 mK and frequency $\nu = 7.3$ GHz, the thermal occupation number is 2.4×10^{-8}, resulting in a negligible dark count rate.

However, present-day devices do not reach this figure due to technical issues such as inefficient thermalization of the microwave field at millikelvin temperatures limiting the effective electromagnetic temperature around 40 mK (see the Appendix) and the presence of out-of-equilibrium quasiparticles in superconductors [18–20]. Nonetheless, even with realistically achievable dark count rates $\Gamma_{\mathrm{dc}} \sim$ 100 s^{-1} and $\eta \sim 0.5$, scan rate enhancements $\mathcal{R} \sim 20$ can be obtained as shown in the present work.

The potential of microwave photon counting has been recently demonstrated in the field of dark matter search with quantum nondemolition measurements of cavity photons, using a device based on a transmon qubit coupled to the signal 3D cavity and to another 3D cavity for signal readout [21]. In this method, the noise has been reduced to the background photons $\bar{n}_{\mathrm{th}} = 7.3 \times 10^{-4}$ compared to $\bar{n}_{\mathrm{SQL}} = 1$ at SQL, corresponding to a projected scan speed enhancement by a factor of approximately 1300.

For axion search, however, a large magnetic field must be applied to the axion cavity, which makes it difficult to integrate the transmon. In this work, we take a different approach by spatially separating the axion cavity from the detector, using a transmon-based SMPD which can count photons propagating in a coaxial cable. This makes it possible to perform an axion search in magnetic fields up to 2 T while still obtaining state-of-the-art dark count rates of less than 100 s^{-1}.

II. SETUP AND PROTOCOL

The present haloscope is based on a hybrid surfaced cylindrical NbTi-copper cavity [22], mounted to the base stage of a dilution refrigerator at 14 mK. At the maximum applied field of 2 T, we measure $Q_0 = 0.9 \times 10^6$ for its axion-sensitive TM_{010} mode. Its frequency can be varied within a few megahertz around 7.37 GHz by a system of three 1-mm-diameter sapphire rods controlled by a cryogenic nanopositioner. The cavity TM_{010} mode is read out by a fixed antenna with coupling coefficient $\beta = 3$; thus, the loaded quality factor is $Q_L = Q_0/(1+\beta) = 2.25 \times 10^5$ in the overall frequency range investigated in the present work. The expected axion signal power is at the 10^{-24} W level (see the Appendix). A circulator routes pulses from input lines toward the cavity for calibration of the cavity parameters and the photons leaking out of the cavity toward the input of the SMPD [see Fig. 1(a)].

The SMPD is a superconducting circuit with a transmon qubit coupled to two resonators: a “buffer” resonator, whose frequency ν_b can be tuned to the incoming photon frequency by applying a magnetic flux to an embedded SQUID, and a “waste” resonator with fixed frequency ν_w. In this circuit, an itinerant photon entering the buffer resonator is converted with close to unit efficiency into a qubit excitation ν_q and a waste photon via a four-wave-mixing (4WM) process [23] activated by a pump pulse at frequency ν_p such that $\nu_p + \nu_b = \nu_q + \nu_w$, corresponding to the energy conservation throughout the 4WM process. The waste resonator quickly damps its converted photon in the environment, ensuring the irreversibility of the 4WM process and forcing the qubit to remain in its excited state. The qubit state is then measured using the dispersive readout method [24]. If it is found in its excited state, then a click of the detector is recorded and the qubit is reset in its ground state. These operations are repeated in cycles of 17 μs on average yielding to measurement records of click arrival time as displayed in Fig. 1(d). This type of detector also finds applications in magnetic resonance [25], and, in particular, it recently enabled single-electron-spin detection [26].

Axion dark matter experiments search for a power excess above a background that must be reliably estimated at each cavity frequency. For the present counting experiment, we adopt a measurement strategy used in astrophysics or high-energy experiments [27], whereby an observation potentially containing a new source or effect (“on” measurement) is contrasted with a background-only observation free of

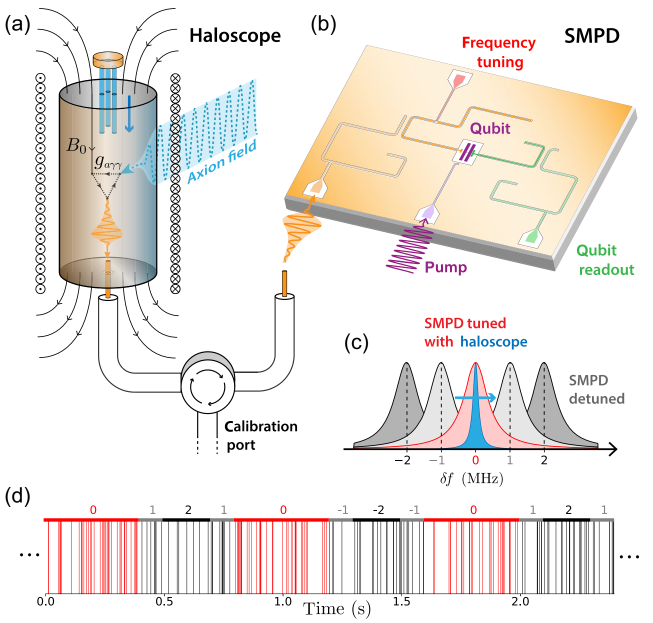

FIG. 1. Schematic of the axion search setup. (a) The haloscope cavity, located in a 2T magnet, connects to the detector via a fixed antenna port and features cryogenic frequency tuning through three sapphire rods attached to a nanopositioner. (b) The SMPD, a superconducting circuit with $\lambda/2$ coplanar waveguide resonators linked to a transmon qubit, is positioned approximately 50 cm above the magnet and connects via standard coaxial cables. Its frequency is adjustable by threading the flux through a SQUID embedded in the buffer resonator. Upon activating the four-wave mixing process, the qubit cycles through photon detection phases. (c) The detector center frequency alternates between resonance (red) and off-resonance (gray) settings relative to the haloscope's frequency (blue) in differential mode. (d) Measurement records from the photon counter display clicks over time, with color indicating the detector's frequency setting. Labels $0, \pm 1, \pm 2$ above the graphical representation of individual photon arrival times indicate that the frequency of the buffer resonator has been set to ν_c, $\nu_c \pm 1$ MHz, and $\nu_c \pm 2$ MHz, respectively.

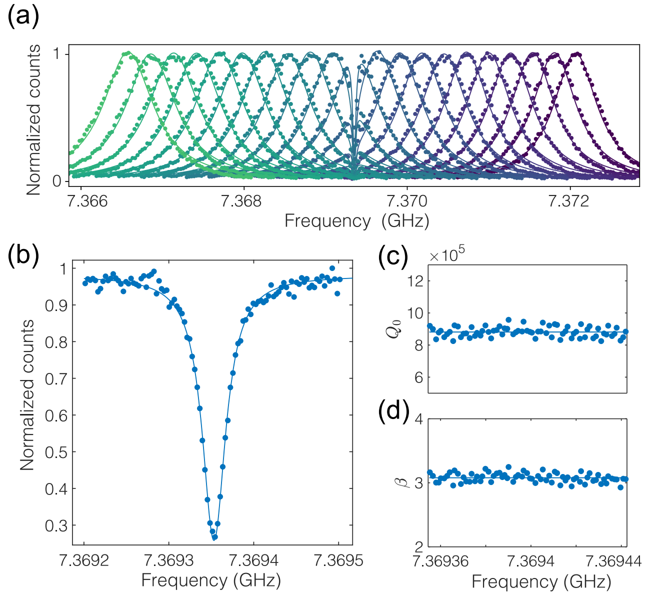

FIG. 2. Microwave cavity reflection spectroscopy using a photon counter. (a) The SMPD response to a continuous calibration tone is plotted as a function of frequency. While the SMPD bandwidth is 0.7 MHz, its center frequency can be tuned over a range exceeding 100 MHz by threading magnetic flux through the SQUID loop. Here, the SMPD is tuned across a 5 MHz span centered around the haloscope frequency, which appears as a dip in the measured counts—a signature of the absorption of the haloscope cavity measured in reflection (see the Appendix). (b) To estimate the cavity parameters Q_0 and β, the SMPD frequency is swept across the haloscope resonance. (c),(d) The measurements of the cavity parameters are repeated cyclically as part of the quantum protocol during cavity frequency scans. For the interval $[7.369355 - 7.369442]$ GHz, the quality factor is determined to be $Q_0 = (8.8135 \pm 0.31) \times 10^5$, and the coupling coefficient is $\beta = 3.08 \pm 0.07$. These parameters remain approximately constant across the scanned frequency range. Horizontal lines represent the average values of Q_0 and β across $N = 72$ measurements.

the effect ("off" measurement). We, therefore, estimate the background by recording off-resonance clicks when ν_b is detuned by ± 1 and ± 2 MHz and the source plus background when $\nu_b = \nu_c$.

To explore different axion masses, the cavity frequency ν_c is tuned during the quantum sensing protocol, with parameters ν_c, loaded quality factor Q_L, and coupling β to the transmission line being monitored periodically with the SMPD (see Fig. 2).

The detector efficiency η is measured by monitoring the count rate of the detector while applying a microwave tone at its input, whose power is calibrated by measuring the ac-Stark shift and photon-induced dephasing of the transmon qubit (see the Appendix). We measure an operational efficiency $\eta = 0.47 \pm 0.013$ on average including dead times and imperfections of the SMPD. We observe efficiency fluctuations on a timescale of minutes of the order of $\pm 10\%$ mainly due to slow drifts of the flux threading the detector SQUID loop as well as fluctuations of the transmon qubit relaxation time [20].

III. DATA ANALYSIS AND SMPD DIAGNOSTICS

The counts acquired as described in the previous section are then grouped into resonance and off-resonance counts. Because of the chosen quantum protocol structure, the acquisition duration at frequency step is 28.6 s at resonance and $7.15\text{s} \times 4 = 28.6$ s at sideband frequency. Over the long timescales required in cavity haloscope searches, the SMPD dark count rate is nonstationary with variations within 10% as shown in Fig. 3(b). We observe that about 600–700 clicks are recorded in 7.15 s on each sideband frequency, while about 2700–2900 on-resonance clicks are registered for 28.6-s-duration intervals. These clicks are originating from photons present at the SMPD input due to an effective temperature of the input line and only to a

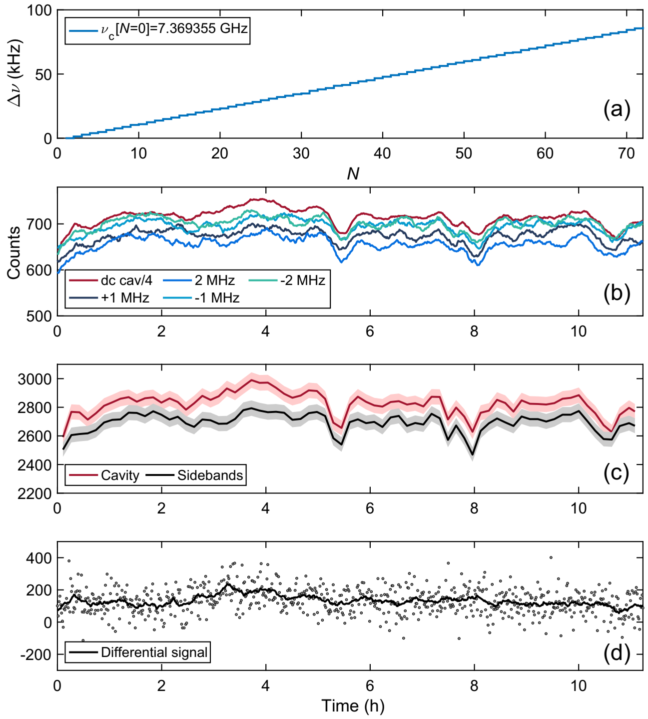

FIG. 3. A selection of data taken at about 5 kHz/h frequency tuning speed, corresponding to the cavity frequency range [7.369355–7.369442] GHz. (a) The cavity frequency changes linearly with cycle number ($N = 72$ in this run). (b) Counts recorded with SMPD buffer $\nu_c \pm 1$ MHz, $\nu_c \pm 2$ MHz, and at resonance. Each data point represents counts recorded in 7.15 s at sideband frequency. For comparison, the counts recorded at resonance have been divided by a factor of 4. (c) Sideband counts are summed to obtain a single series of data that is compared to counts recorded at resonance ($\nu_b = \nu_c$). The $\pm\sigma$ belts indicate the statistical uncertainty expected for Poissonian counts.

minor extent from spurious excitation of the transmon qubit in the absence of incoming photons [20]. The sum of the counts associated with the four sidebands is an estimator of the background B, that can be compared with on resonance counts in the same 28.6-s-duration time window as shown in Fig. 3(c), where a correlation between the two measured quantities is evident. Both the counts registered at cavity frequency [$\nu_b = \nu_c$, labeled with 0 in Fig. 1(d)] and sidebands [$\nu_b = \nu_c \pm 1$ MHz or $\nu_b = \nu_c \pm 2$ MHz, labeled with $\pm 1, \pm 2$ in Fig. 1(d)] vary beyond statistical uncertainty expected for Poissonian counts, as indicated by the $\pm 1\sigma$ belts. If $\{t_i\}$ is the set of click arrival times t_i, we indicate with N_c and N_b the number of the cavity and background clicks, respectively. The difference between the cavity N_c and background counts N_b [see Fig. 3(d)] in the overall 0.4 MHz probed frequency range is unrelated to any dark matter signal inasmuch as it is independent of the cavity frequency, as detailed in the following. This excess at the cavity frequency is instead ascribed to a slightly higher temperature for the cavity resonator compared to the SMPD temperature. In the data analysis, this difference is treated as a bias k_b.

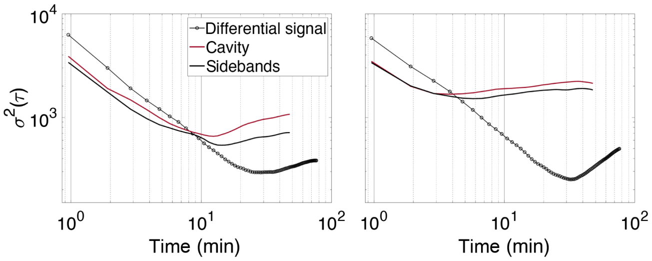

FIG. 4. Excess counts at cavity frequency obtained by the difference between cavity and sideband counts. The thick black curve is obtained by computing the mean over a sliding window of 20 min. Allan variance calculated for data recorded at fixed cavity frequency and for the data displayed in Figs. 3(c) and 3(d).

The SMPD long-term stability can be assessed by calculating the Allan variance for N_c and N_b (see Fig. 3). The click number fluctuations is computed as function of the total integration time τ. At early times, the Allan variance decreases as $1/\tau$, but after only a few minutes it increases again, indicating that a random walk contribution to the click rate comes into play. However, the Allan variance of the difference $N_c - N_b$ follows the $1/\tau$ trend up to a much longer time interval $\tau \sim 30$ min, suggesting that there are common processes affecting the counter operation. At least two mechanisms can explain the observed correlations between N_c and N_b: slow fluctuations of the SMPD efficiency η possibly due to fluctuations of the transmon qubit relaxation time [28] and drifts of the effective temperature of the background photon source, for instance, due to imperfect thermalization of microwave components in the line. The temporal scale of these fluctuations is much longer than the duration of measurements with the SMPD tuned at resonance (N_c) and off resonance N_b (approximately 100 ms). Moreover, the plots in Fig. 4 show that there is no additional noise in the data recorded between successive step motion intervals compared to those acquired with the cavity unperturbed for several hours.

IV. AXION DARK MATTER SENSING

The clicks recorded with SMPD frequency tuned at the cavity frequency and those at sideband frequency can be used not only to learn about the long-term stability of the SMPD, but also to obtain an upper limit on the axion-photon interaction $g_{a\gamma\gamma} = g_\gamma \alpha f_a^{-1}/\pi$, where α is the fine structure constant and f_a is the scale of the breaking of the Peccei-Quinn symmetry, with $f_a/10^{12}$ GeV $= 5.691$ μeV$/m_a$ [9].

The system has been investigated for 12 h at fixed cavity frequency and for an overall range of about 420 kHz centered at 7.3695 GHz by tuning the cavity frequency at about 4.5–5 kHz/h, as heating introduced at the 15 mK stage by the currents needed to drive the nanopositioner

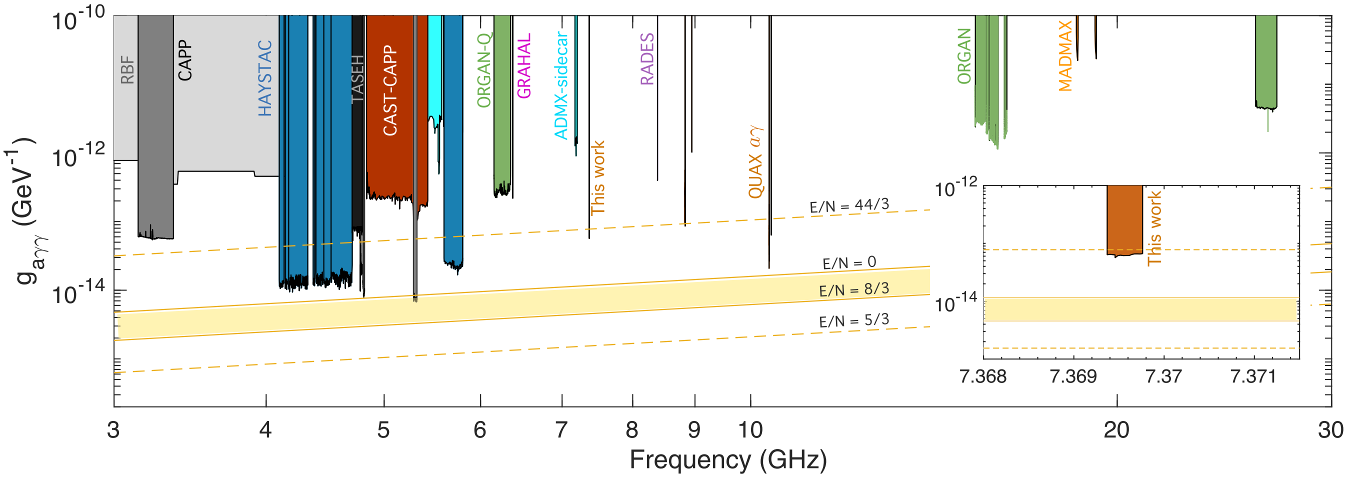

FIG. 5. (a) Constraints on axion-photon coupling: haloscopes closeup in the range 3–30 GHz showing the limit obtained in the present work alongside results from RBF [29], CAPP [30–33], HAYSTAC [34–37], TASEH [38], CAST-CAPP [39], ADMX-sidecar [40], ORGAN [41–43], GrAHal [44], RADES [45], QUAX$a\gamma$ [22,46–49], and MADMAX [50]. The bounds represented by the dotted lines enclose the region of parameter space of phenomenologically preferred axion models [51], extending beyond the commonly assumed QCD axion window (yellow band). E and N are, respectively, the electromagnetic and QCD anomaly coefficients, setting the axion-photon coupling constant $g_{a\gamma\gamma} = (\alpha/2\pi f_a)(E/N)$ [52]. (b) Exclusion limit at 95% confidence level on the axion mass coupling parameter space. We obtain an upper limit on the axion-induced power that translates to an upper limit on $g_{a\gamma\gamma}$ for $m_a \in [30.477, 30.479]$ μeV, corresponding to a cavity frequency window of 0.4 MHz centered around 7.3696 GHz. Exclusion limits are taken from Ref. [53].

degraded the SMPD sensitivity for tuning speeds above approximately 12 kHz/h. The probed frequency range corresponds to 14 cavity linewidths, each providing independent values of N_b and N_c useful for the dark matter search. Clearly, the measurement time Δt spent probing $[\nu_c, \nu_c + \Delta\nu_c]$, with $\Delta\nu_c = 32$ kHz, largely exceeds τ_m; thus, we select a subset of data to optimize the haloscope speed. Each Δt has been divided into subintervals of duration $\Delta t_m = 10$ min, and the interval with the maximum SMPD sensitivity, i.e., having the lowest cavity counts $N_c^\star$, was selected to devise the plot in Fig. 5.

In each subinterval, the counts' mean equals their variance as expected for Poissonian statistics; therefore, to infer the upper limit we can apply the maximum likelihood ratio test to assess the significance of an excess at the cavity frequency [27]. In the recorded data, we observe that, for the selected minimum cavity counts $N_c^\star$ in the 10-min-duration subintervals, the corresponding background counts $N_b^\star$ is biased by $k_b = N_c/N_b - 1$, which amount to a few percent on average in the collected dataset. Using the Wilks theorem [27] for large sample size, as is the case for the present data [$O(10^4)$ counts in each subinterval], the significance for $N_c^\star$ counts for each cavity linewidth is given by

$$S = \sqrt{2}\left\{N_b^\star \log\left[\frac{(k_b+2)N_b^\star}{N_b^\star + N_c^\star}\right] + N_c^\star \log\left[\frac{(k_b+2)N_c^\star}{(1+k_b)(N_b^\star + N_c^\star)}\right]\right\}^{1/2}, \tag{1}$$

where we take the same detection efficiency for cavity and background counts.

The required significance to claim a detection is set at 5σ, corresponding to a false alarm probability of approximately 10^{-7} for a Gaussian distribution. In the four acquisition runs, representing 14 cavity linewidths, no significant excess was found assuming a conservative bias value $k_b = 0.05$. Therefore, we set the upper limits $N_{95}^\star$ on source counts at 95% CL (i.e., 2σ significance), by interpreting excess counts $N_{95}^\star - N_b^\star$ as signal power P_{95} due to axion to photon conversion:

$$P_{95} = \eta h\nu_c \frac{N_{95}^\star - N_b^\star}{\Delta t_m}. \tag{2}$$

The upper limit on $g_{a\gamma\gamma}$ obtained from the calculated axion signal power (see the Appendix) and Eq. (1) is reported in Fig. 5 for the probed frequency range.

V. CONCLUSIONS AND OUTLOOK

We devised an axion search protocol for a haloscope equipped with an SMPD, whereby clicks are recorded at both the cavity and the sideband frequency to reliably assess the background noise during the search. Allan variance plots indicate that for the present device the most convenient haloscope integration time is of about 10–15 min. As the inhomogeneity of the Poisson process sets in for temporal intervals much larger than the chosen integration time of 10 min, we are able to give an upper limit $g_{a\gamma\gamma} < 7 \times 10^{-14}$ GeV^{-1} in the mass range (30.477–30.479)μeV.

The exclusion plot we obtained corresponds to a search speed of 4.3 MHz/day. As $\Delta f/\Delta t_m$ is proportional to the $B^4 g_{a\gamma\gamma}^4 V_{\mathrm{eff}}^2$, with $V_{\mathrm{eff}} = C_{010}V$ the effective cavity volume, we can estimate a scan rate exceeding a hundred megahertz per year at the sensitivity required to probe the full QCD axion band for an experiment equipped with a commercially available magnetic field of 12 T in place of the 2 T magnet used in these tests and a state-of-the-art 3D resonator with 10 times as much the effective volume. Compared to a haloscope based on a SQL linear amplifier, in the present scheme photon counting allows for running the search at a speed larger by a factor of $\mathcal{R} = \eta^2 \Delta\nu_a/\Gamma_{\mathrm{dc}} \sim 20$, with the signal linewidth $\Delta\nu_a = 7.3$ kHz, the dark count rate $\Gamma_{\mathrm{dc}} = 85\ \mathrm{s}^{-1}$, and the efficiency $\eta = 0.46$. With realistically achievable dark count rates $\Gamma_{\mathrm{dc}} \sim 10\ \mathrm{s}^{-1}$ and $\eta = 0.8$ scan rate enhancements, $\mathcal{R} \sim 500$ can be obtained.

The gain in scan speed we have demonstrated is currently limited by the dark count rate, which can be further suppressed by narrowing the bandwidth of the input resonator or by improving the thermalization of the lines. The latter can be accomplished for instance using attenuators with improved thermal conduction to the dilution refrigerator stages [54,55].

In addition, we have devised a detection method applicable to broad frequency ranges, as the SMPD input resonator frequency can very rapidly be adjusted to the cavity frequency while the latter is tuned across a few hundred megahertz. Note that a Josephson mixer [56] allows one to virtually expand the bandwidth of the present SMPD to include any cavity haloscope in the interesting, yet unprobed high-frequency range where heavier axions can be detected. Our results demonstrate the potential of microwave photon counting in axion DM searches above 5 GHz frequency, accelerating by more than one order of magnitude the search and significantly simplifying the data acquisition and analysis without losing the required robustness thanks to the employed metrological methods.

ACKNOWLEDGMENTS

We are grateful to E. Berto (University of Padova and INFN), who substantially contributed to the mechanical realization of the cavity and of its tuning system. We thank the sputtering laboratory of the INFN Legnaro Laboratory (C. Pira) for the preparation of the NbTi films on the copper resonators. The contribution of M. Tessaro and F. Calaon (INFN Padova) to the experiment electronics and cryogenics, respectively, is gratefully acknowledged. We acknowledge technical support from P. Sénat, D. Duet, P.-F. Orfila, and S. Delprat from CEA/SPEC and are grateful for fruitful discussions within the Quantronics group. We acknowledge IARPA and Lincoln Labs for providing the Josephson traveling-wave parametric amplifier. This research is supported by the U.S. Department of Energy, Office of Science, National Quantum Information Science Research Centers, Superconducting Quantum Materials and Systems Center (SQMS) under Contract No. DE-AC02-07CH11359, by the MUR Departments of Excellence Grant No. 2023-2027 “Quantum Frontiers”, and by INFN through the QUAX experiment. This project has received funding from the European Union Horizon 2020 research and innovation program under ERC-2021-STG Grant Agreement No. 101042315 (INGENIOUS).

The authors declare no competing interests.

DATA AVAILABILITY

Raw data, analysis codes are available from the corresponding author on reasonable request.

APPENDIX A: SMPD CIRCUIT FABRICATION

First, a 2-inch sapphire substrate is cleaned by dipping it in a 2 : 1 mixture of H_2SO_4 and H_2O_2 during 20 min. The substrate is then loaded in a sputtering machine where a 60-nm-thick tantalum thin film is deposited at 600 °C to favor growth in the α phase. The wafer is then diced into rectangular chips of $10 \cdot 11\ \mathrm{mm}^2$. The patterning of the main elements of the circuit is achieved by wet etching tantalum with Transene 111 through an optically patterned AZ1518 resist mask. The chip is then cleaned by immersing it in successive baths: isopropyl alcohol (IPA), acetone, and 2 : 1 mixture of H_2SO_4 and H_2O_2. Aluminum junctions are made using the Dolan bridge technique. The mask consists of a double-layer PMMA (110 nm)–MAA (1100 nm) resist and a discharging layer of 7 nm of aluminum; it is then patterned using electron beam lithography (at 30 kV). After the exposure, the discharging layer is first removed by immersing the chip in a KOH solution ($10\ \mathrm{g} \cdot \mathrm{L}^{-1}$). The resist is then developed in a 1 : 3 methylisobutylketone-IPA mixture. The chip is then loaded in an electron beam evaporator to make the junctions. The two aluminum layers are evaporated with 28° and −28° angles creating overlaps over a well-defined area, controlled by the mask geometry. The first aluminum layer is 35 nm thick and the second 65 nm thick. Between the two deposition steps, the aluminum is oxidized during 5 min by injecting an argon-oxygen gas mixture into the deposition chamber at a pressure of 10 mbar. Finally, the resist mask is lifted off by immersing the chip in an acetone bath. Then, the junctions are then recontacted to the tantalum circuit with aluminum patches. After coating the chip with an optical resist (Microposit S1805), windows overlapping the junctions and the ground plane areas to be recontacted are opened using optical lithography. The chip is then loaded in an electron-beam evaporator. We first perform an ion milling based on an argon ion beam accelerated at 500 V. Finally, a 100 nm aluminum layer is then deposited on the chip covering the areas etched by the ion milling step. The resist is then removed.

TABLE I. Measured SMPD parameters. χ_{qb} (χ_{qw}) is the dispersive coupling of the buffer (waste) resonator. κ_{ext}, given for both the waste and buffer resonators', is related to their external (coupling) losses, while κ_{int} refers to their internal losses.

Qubit	
ν_q	6.222 GHz
T_1	17–20 μs
T_2^*	28 μs
$\chi_{qq}/2\pi$	240 MHz
$\chi_{qb}/2\pi$	3.4 MHz
$\chi_{qw}/2\pi$	15 MHz
Waste mode	
ν_w	7.9925 GHz
$\kappa_{\mathrm{ext}}/2\pi$	1.0 MHz
$\kappa_{\mathrm{int}}/2\pi$	< 100 kHz
Buffer mode	
ν_b	7.3693 GHz
$\kappa_{\mathrm{ext}}/2\pi$	0.48 MHz
$\kappa_{\mathrm{int}}/2\pi$	40 kHz

APPENDIX B: SMPD CIRCUIT PARAMETERS

In Table I, the measured SMPD parameters are reported.

APPENDIX C: QUANTUM SENSING PROTOCOL

The quantum sensing sequence consists of nested cycles as follows (see also Fig. 8).

(i) The detection cycle begins with a 10.5 μs pump pulse applied to the qubit port to activate the 4WM process, followed by a 0.8 μs readout pulse directed to the waste port. The qubit is then reset utilizing the real-time feedback capabilities of the system controller resulting in a latency of 0.7 μs that includes electrical delay, signal processing, and Field-Programmable Gate Array (FPGA) latency. If the qubit is in its ground state, an additional 0.3 μs waiting time is imposed before the cycle restarts. If the qubit is in its excited state, a 0.2 μs qubit π pulse is applied, followed by a 0.8 μs readout pulse. This reset procedure continues until successful. The detection cycle time varies, with an average duration of 12.4 μs.

(ii) To change the SMPD frequency, a slow flux ramp is applied for 0.72 ms, followed by a 0.1 ms pause to mitigate potential heating. Subsequently, dark counts are logged over 8001 detection cycles (input on), yielding an average time of 99.075 ms. The detector's efficiency (no input) is assessed over 801 detection cycles by evaluating the SMPD count rate with a calibrated microwave pulse in use. This efficiency assessment averages 9.91 ms per cycle.

(iii) Sequence (ii) is repeated for buffer frequencies ν_b matching the cavity frequency, identified as 0, $\nu_c \pm 1$ MHz (labeled as $1, -1$), and $\nu_c \pm 2$ MHz (labeled as $2, -2$). This arrangement facilitates the recording of dark counts for equal durations when at and away from cavity resonance $(0\,0\,1\,2\,2\,1\,0\,0\,0\,0-1-2-2-1\,0\,0)$, thus halving the haloscope detector's duty cycle to 50%. This sequence design ensures all flux ramps share identical amplitude to circumvent systematics related to spurious heating.

(iv) A minimal nanopositioner voltage pulse is applied, followed by a 5 s waiting period. Then, sequence (iii) is executed $N_r = 36$ times. This cycle (iv) spans an average of 78 s, covering sequence loading, data collection, and data saving phases.

(v) Cycle (iv) is reiterated 10 times, interspersed with a calibration sequence lasting 78 s, initiated by a subtle nanopositioner voltage pulse to evenly distribute nanopositioner voltage pulses over time and prevent slow thermal fluctuations. The calibration process is twofold. Initially, the haloscope frequency is determined by gauging the photon count reflected from the haloscope cavity across various illumination frequencies using the SMPD. A Lorentzian fit to the haloscope power absorption curve provides an accurate frequency estimate ν_c of the haloscope, down to subkilohertz precision. Next, the SMPD's central frequency and bandwidth are gauged across different bias voltage levels close to the operational point to adjust for low-frequency magnetic flux drifts. Subsequently, the SMPD's central frequency is aligned with the newly measured haloscope frequency. Additionally, a list of bias voltage values is compiled for adjusting the buffer frequency to ν_c (0), $\nu_c \pm 1$ MHz $(1, -1)$, and $\nu_c \pm 2$ MHz $(2, -2)$.

(vi) Cycle (v) is executed continuously, ensuring a consistent operation flow. The active measurement time dedicated to haloscope observation within cycle (v) amounts to $99.075\ \mathrm{ms} \times 36 \times 8 \times 10 = 285$ s, equivalent to 4.76 min. This duration is intentionally mirrored for the SMPD background measurement to maintain the differential mode operation of the SMPD-based axion search. Consequently, the total span of cycle (v) averages to 920 s or approximately 15.3 min. Within this time frame, approximately 350 s are identified as dead times per cycle, accounting for about 38% of the total cycle duration. This segment includes critical operations like efficiency verifications and frequency adjustments alongside other less crucial intervals for tasks such as extended waiting periods, data processing, and saving. Opportunities to refine and reduce these dead times will be explored in subsequent experimental setups, aiming for enhanced efficiency and throughput.

APPENDIX D: EFFICIENCY CALIBRATION

The calibration of the SMPD is conducted by measuring the dephasing and ac-Stark shift of the qubit, which is induced by the illumination of the input resonator of the SMPD with a weak coherent tone. This calibration is carried out without any pump tone, and, thus, the SMPD is treated merely as an elementary component of a circuit quantum electrodynamics system. In this setup, the qubit is dispersively coupled to the input resonator, following the Hamiltonian in the rotating frame of the coherent drive:

$$\hat{H}/\hbar = \Delta\hat{a}^\dagger\hat{a} + \frac{\omega_\mathrm{q}}{2}\hat{\sigma}_z - \frac{\chi}{2}\hat{a}^\dagger\hat{a}\hat{\sigma}_z + \epsilon(\hat{a}^\dagger + \hat{a}), \qquad \text{(D1)}$$

where ω_q represents the qubit angular frequency, χ the qubit dispersive shift, Δ the detuning between the coherent drive and the resonator frequency, and ϵ the coherent drive rate of the resonator.

The qubit, influenced by the coherent drive, experiences a frequency shift corresponding to the average number of photons in the cavity, while photon number fluctuations lead to a qubit dephasing also dependent on the photon number.

Following the method detailed in Ref. [24], the angular frequency shift $\delta\omega$ and dephasing $\delta\gamma$ are directly linked to the coherent complex amplitudes α_g and α_e of the photon field inside the resonator induced by the coherent drive, for the qubit in its ground and excited states, respectively, as given by the expression

$$\delta\omega + i\delta\gamma = -\chi\alpha_g\overline{\alpha_e} = \frac{-4\chi|\epsilon|^2}{(\kappa + i\chi)^2 + 4\Delta^2}, \qquad \text{(D2)}$$

where κ is the dissipation rate of the resonator. The coherent complex amplitudes are defined as

$$\alpha_{g/e} = \frac{\epsilon}{\kappa/2 + i(\Delta \mp \chi/2)}. \qquad \text{(D3)}$$

The qubit frequency shift and dephasing are experimentally measured by performing a Ramsey experiment on the qubit, varying the frequency of the coherent drive applied to the cavity. The measured quantities, which include qubit decay rates and frequency shift, are plotted as a function of the frequency detuning of the coherent drive. The dispersive shift χ and the cavity decay rate κ are extracted from the overall shape of the curve, with ϵ serving as the frequency scaling parameter.

The power of the coherent drive at the input of the cavity is calculated using input-output relations:

$$P_\mathrm{in} = \hbar\omega_0\frac{|\epsilon|^2}{\kappa - \kappa_\mathrm{l}}, \qquad \text{(D4)}$$

where κ_l is the rate of the resonator loss channel, measured independently through reflectometry using a vector network analyzer. The power input, expressed in units of photon flux, is $P_\mathrm{in}/\hbar\omega$. The error bars are computed from statistical uncertainty associated from the data shown in Fig. 10.

As illustrated in Fig. 10, this calibration process determines that the photon flux at the input of the resonator for the calibration coherent tone is $P_\mathrm{in}/\hbar\omega = 20050 \pm 340$ photons s^{-1}, or, in power units, $P_\mathrm{in} = 0.979 \pm 0.016 \times 10^{-19}$ W.

With the input tone calibrated, the operational efficiency of the SMPD, based on the four-wave-mixing process and including duty cycles and dead times, is assessed by measuring the click rate of the device over a minute while continuously illuminated with the calibrated coherent tone. This process reveals an excess click rate over the background dark count of 9233 ± 30 clicks s^{-1}, leading to an efficiency of $\eta = 0.460 \pm 0.009$. Note that, due to fluctuations in the relaxation time of the qubit typical of transmon circuits, a slow drift of the efficiency is expected on hour timescales; this is why the count rate is continuously monitored during the cycle (ii) of the haloscope measurement.

APPENDIX E: BASIC CHARACTERIZATION OF THE SMPD

The readout of the SMPD utilizes the standard dispersive readout method. A 0.8 μs coherent pulse is directed onto

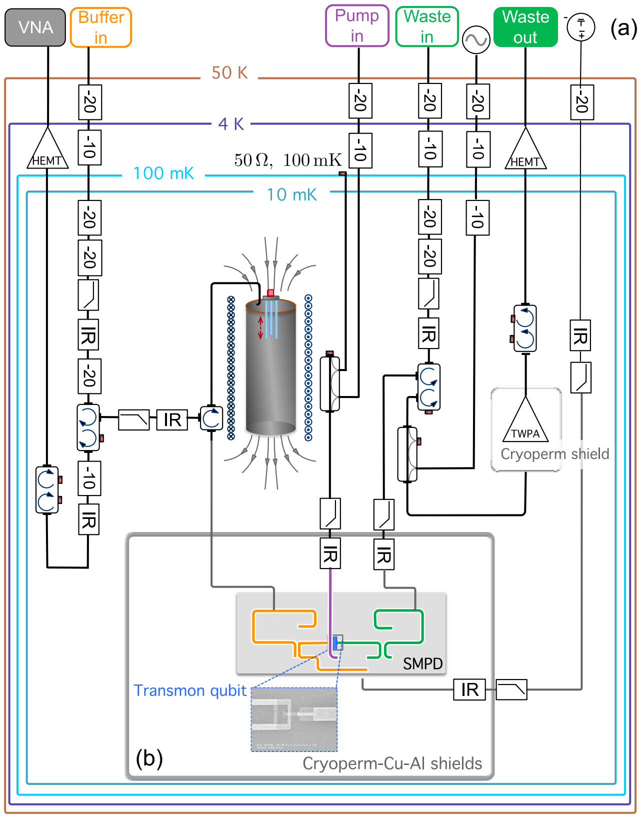

FIG. 6. (a) Schematic cabling of the dilution refrigerator. (b) The SMPD is enclosed in a box made with three screens (Al, Cu, and cryoperm), while the traveling wave parametric amplifier (TWPA) is within a separate cylindrical cryoperm shield.

the waste resonator (in Fig. 6, at port labeled "Waste in") at its resonant frequency when the qubit is in its excited state ($\omega_w - \chi_{qw}$). The reflected signal, encoding the qubit state's complex amplitude, is amplified (line "Waste out" in Fig. 6) by a Josephson parametric traveling wave amplifier at base temperature, followed by a high electron mobility transistor amplifier at 4 K and a low noise amplifier at room temperature. This signal is then demodulated and integrated into a voltage reading, which is compared against a threshold to determine a click event in the SMPD. Figure 7 displays the integrated voltage as a function of the qubit state. From these data, we determine the readout fidelity of the qubit when it is in its excited state as $p(1|e) = 0.93$, and the thermal equilibrium population of the qubit in its resting state as $p_{\mathrm{th}} = 2 \times 10^{-4}$. Additionally, the readout fidelity for the ground state is estimated through consecutive measurements, revealing that the probability of incorrectly identifying the qubit's ground state is less than 5×10^{-5}.

The four-wave-mixing process is calibrated by measuring the probability of the qubit's excited state while simultaneously illuminating the detector with a pump tone at the matching frequency for four-wave mixing and a coherent tone at the input resonator frequency. As shown in Figs. 10(a) and 7(b), by adjusting the frequencies of these two tones, we identify the optimal conditions where the excited state probability is maximized. We further confirm the accuracy of the mixing process by observing the disappearance of the excited state population when the coherent drive at the input resonator is deactivated. The input resonator's frequency is made adjustable by incorporating a SQUID at its voltage node. The resonator frequency is modulated by applying a magnetic flux through the SQUID. This adjustment ensures that the

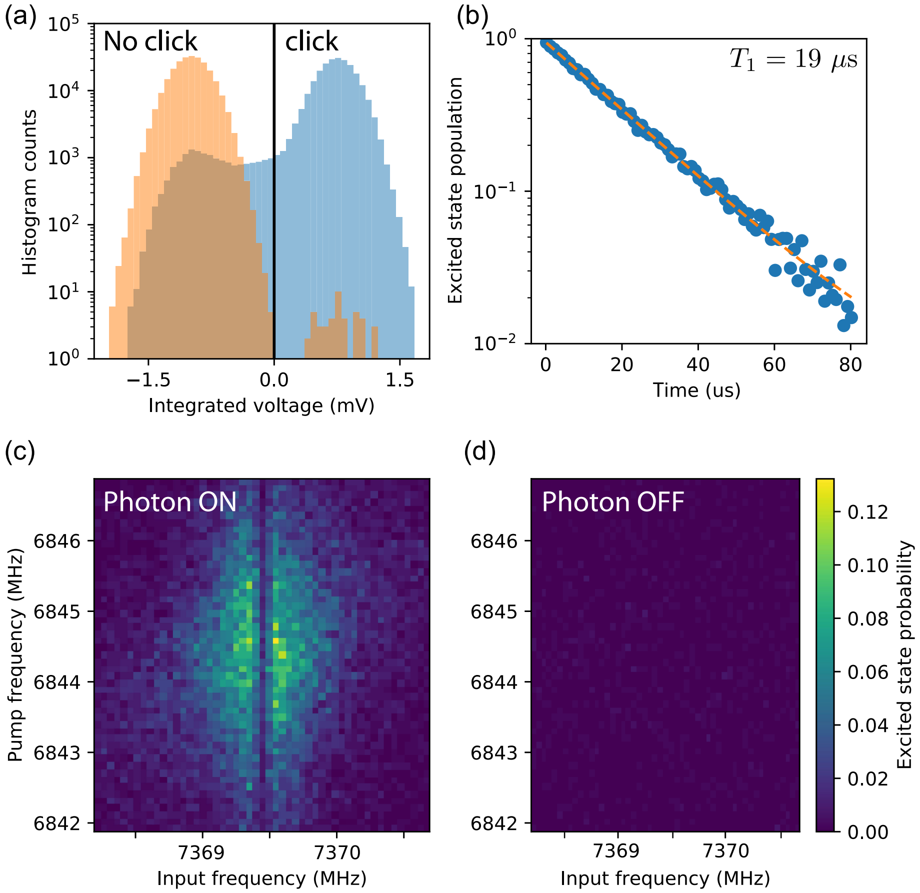

FIG. 7. SMPD characterization. (a) Readout histogram of the transmon qubit measurement. Readout fidelity for the excited state is 0.93, while the ground state readout infidelity is less than 5×10^{-5}. The thermal equilibrium population of the qubit is $p_{\mathrm{th}} = 2 \times 10^{-4}$. (b) Relaxation measurement of the transmon qubit indicates a T_1 value of 19 μs. (c) Pump frequency tuning involves measuring the qubit state population while driving the pump and a coherent tone on the input resonator. Optimal working points are identified by varying the frequencies of the two drives. The dark band corresponds to absorption of the input tone photons at the cavity frequency. Cavity off-resonance frequencies are instead reflected at the cavity port and, thus, are routed by the circulator to the buffer resonator. (d) With the coherent tone turned off, the qubit population remains close to zero, confirming that the correct four-wave-mixing process is at play.

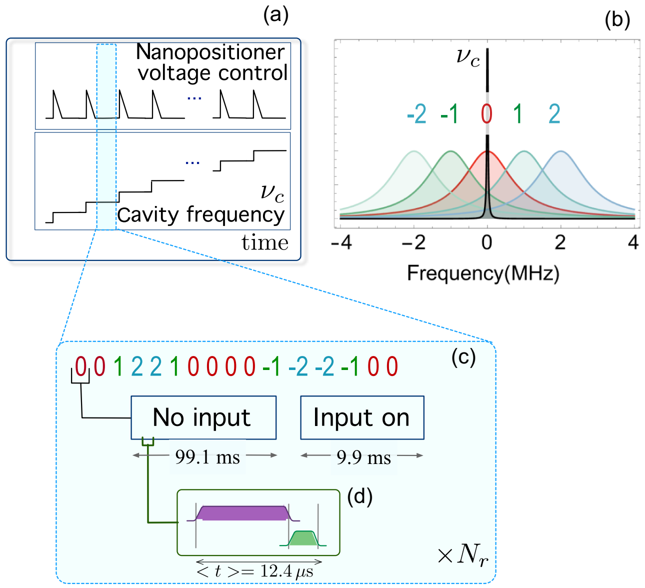

FIG. 8. (a) We tune the cavity by displacing dielectric rods inside the cavity's volume with a linear z nanopositioner driven by a sawtooth voltage. (b) Values of ν_b set within the protocol. Labels – 2, −1, 1, and 2 indicate that clicks are recorded with ν_b differing from the cavity frequency of resonance $\nu_c = \nu_c$ by the label numerical value given in megahertz. "0" corresponds to the resonance condition $\nu_b = \nu_c$. To monitor the counter detection efficiency, white noise is injected during the "input on" phase at the buffer input, while with the counts recorded in the "no input" phase the operational dark count can be assessed under different experimental conditions. (c) The buffer frequency ν_b is cycled through the sequence shown for $N_r = 36$ times. Before each cycle, a tuning step is devised, in which a weak voltage pulse is applied to the nanopositioner, followed by 5-s-duration waiting time. (d) The detection cycle includes a 10.5-μs-duration pump pulse (violet), followed by the readout time (green), which is not deterministic. The average duration of this block is 12.4 μs.

resonator's frequency aligns with the haloscope frequency for effective four-wave mixing. The presence of a dark line in Fig. 10(a), indicative of the absorption of photons resonant with the haloscope, validates that the SMPD is correctly tuned to the haloscope.

APPENDIX F: FREQUENCY CALIBRATION ROUTINE

This section details the calibration routine executed in each cycle (v), performed every 920 s and typically lasting 78 s.

1. SMPD frequency routine

In the frequency calibration routine, we assess the excited state population of the qubit as it relates to the frequency of the coherent drive on the input resonator, spanning 3 MHz.

A 2 mV span voltage bias is applied to control the magnetic flux through the SQUID, thereby altering the input resonator frequency by approximately ±3 MHz. The results, as depicted in Fig. 11, are presented in a color plot, detailing the relative detuning in comparison to the expected frequency of the input resonator. In Fig. 11(c), the data are shown based on the absolute driving frequency of the input resonator. Key detuned SMPD bias points, such as ±1 MHz and ±2 MHz (targeted for background measurements), are highlighted by vertical lines. The dataset demonstrates a consistent response of the SMPD across a broad frequency range. Through meticulous analysis, we adjust the pump and flux bias for each scanning frequency, countering slow magnetic drifts in the SQUID bias, which is recalibrated every 15 min.

2. Haloscope frequency routine

As established earlier, the SMPD's capability to scan frequencies beyond its linewidth, while maintaining steady efficiency, enables reflection spectroscopy of the haloscope, independent of the SMPD's linewidth. In this process, shown in Fig. 11(b), the SMPD's click rate is recorded while the coherent drive frequency is scanned across a 0.3 MHz range centered on the haloscope's anticipated resonance frequency. This method ensures a uniform SMPD response as both the SQUID bias and pump frequency are concurrently adjusted. The resultant detailed absorption spectrum of the haloscope is fitted with a Lorentzian curve, from which we extract the haloscope's frequency and linewidth with remarkable subkilohertz precision.

3. Resolving the beta factor ambiguity of the haloscope

The SMPD's reflection spectrum exclusively reflects the magnitude of the reflection coefficient, leaving an inherent ambiguity: Identical spectra can result from distinct beta factors, signifying either an overcoupled ($\beta > 1$) or undercoupled ($\beta < 1$) state. To resolve this uncertainty, one could analyze the pulsed response of the cavity over time and across frequencies. However, the SMPD's time resolution, limited by its 10 μs detection window, necessitates a reduction in the detection window duration to 1 μs to improve resolution, albeit at the cost of reduced duty cycle (28%). Figure 12 showcases the SMPD's click rate in response to an 80 μs pulse applied to the haloscope, with the excitation pulse frequency spanning a 200 kHz range centered around the haloscope's frequency and the SMPD frequency adjusted accordingly. This measurement conclusively indicates that the haloscope's temporal response is consistent only with an overcoupled configuration ($\beta = 3.1 > 1$).

APPENDIX G: MICROWAVE 3D RESONATOR

The 3D resonator where axions might convert to photons is a clamshell cavity of cylindrical body 128 mm long and with 31.64 mm diameter, closed with 10-mm-long conical

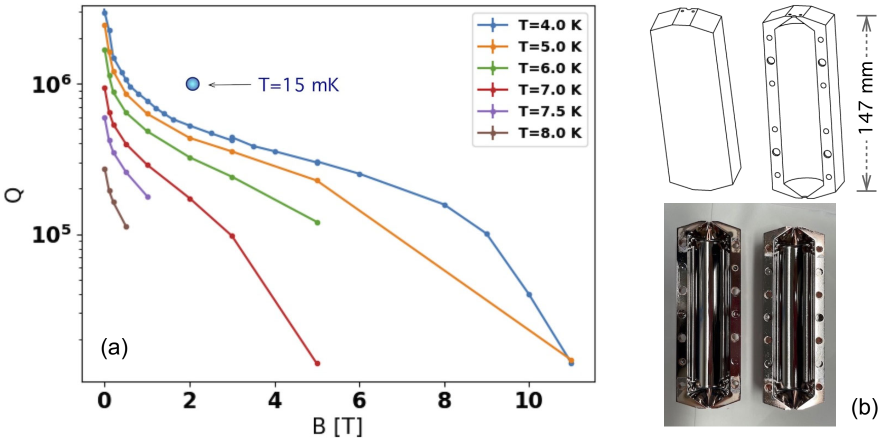

FIG. 9. (a) Microwave cavity quality factor Q_0 versus applied magnetic field for a few temperature values, as measured in a helium flow cryostat. The blue dot is the quality factor measured at 2 T field at about 15 mK temperature. (b) Cavity geometry, realized in two hollowed-out copper bodies. Only the central cylindrical part is covered with a superconducting NbTi film. The cavity end caps are shaped as cones.

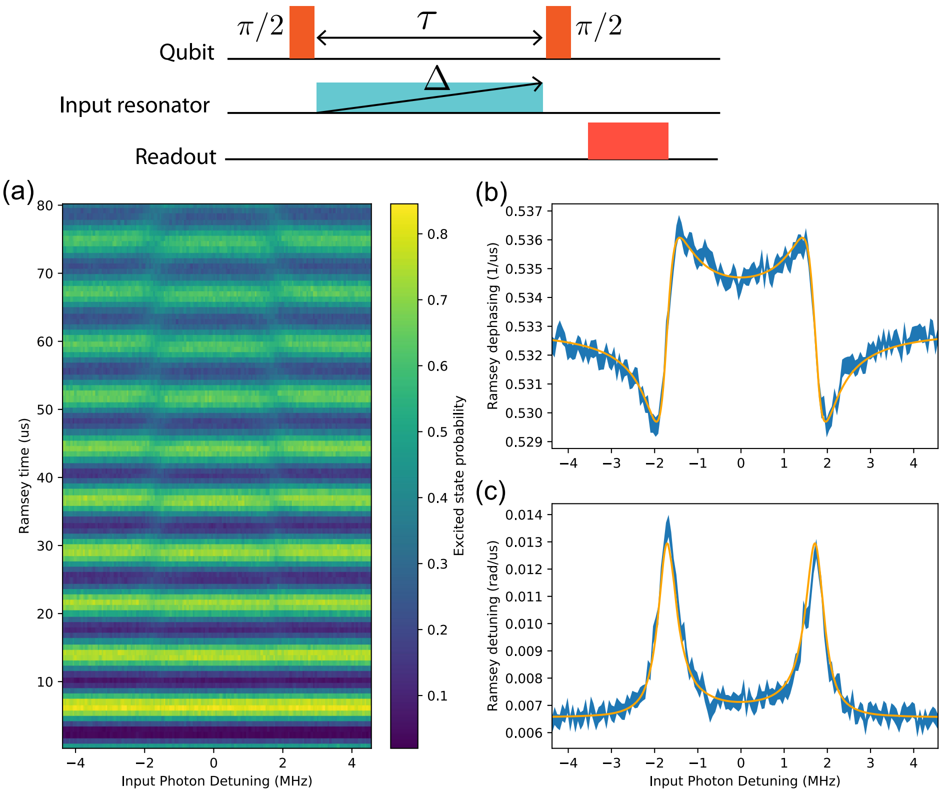

FIG. 10. Coherent tone calibration by Ramsey measurement under illumination. The pulse sequence consists of two $\pi/2$ pulses separated by a Ramsey interval τ. A coherent drive populates the input resonator during the waiting time. Following the sequence, the qubit is read out. (a) Qubit population as a function of the waiting time and the frequency of the coherent drive. Ramsey oscillations are observed in the qubit population. When the drive resonates with the input resonator, both a frequency shift and an accelerated decay of the Ramsey oscillations occur. (b),(c) Simultaneous determination of the frequency shift and decay rate as a function of drive detuning (blue line) by fitting individual Ramsey traces. The width of the line represents the uncertainty in the fit results. The orange line corresponds to the theoretical model described in the main text, enabling the determination of the resonator decay rate ($\kappa/2\pi = 0.523 \pm 0.014$ MHz), the dispersive shift ($\chi/2\pi = 3.461 \pm 0.015$ MHz), and the coherent drive rate ($\epsilon/2\pi = 40.9 \pm 0.5$ kHz).

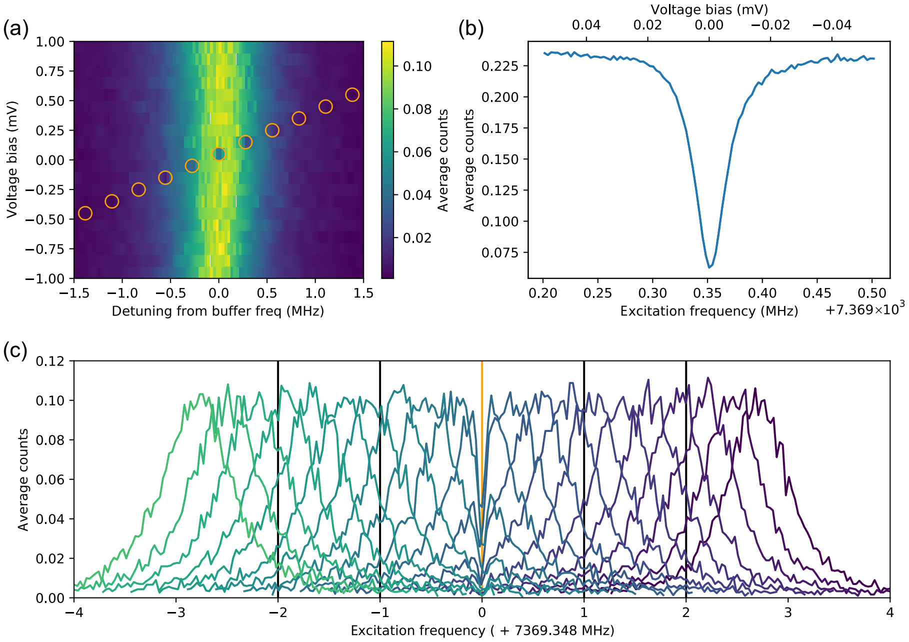

FIG. 11. Frequency calibration routine. (a) The click count is measured as a function of the SQUID bias voltage and the detuning between the coherent drive and the expected input resonator frequency at each SQUID bias voltage. Pump frequency adjustments accompany each SQUID bias voltage change. (b) The same data presented as a function of the absolute frequency of the coherent drive. Note the sharp decrease in the count number [circled in orange in (a)], indicating the absorption by the haloscope cavity. (c) Both the SMPD frequency and the coherent drive frequency are scanned across the haloscope resonance. The absorption dip observed in the reflection coefficient enables the determination of the haloscope's frequency and linewidth.

end caps to reduce current dissipation at copper interfaces. The two halves are machined from oxygen-free high thermal conductivity copper, treated with electrochemical polishing before deposition of a superconducting NbTi film by magnetron sputtering. As a type-II superconductor, below its critical temperature NbTi is not in the Meissner state but rather in the vortex state, with partial penetration of the magnetic flux in the material. The dissipation mechanism is vortex motion; thus, to minimize the overall cavity surface resistance R_s, only the cylindrical body, where the currents of the mode TM_{010} are parallel to the applied field, is covered by the NbTi film. The internal quality factor Q_0, inversely proportional to R_s, deteriorates with increasing static B field amplitude as shown in Fig. 9, where measurements of Q_0 made with a twin cavity are reported. This cavity differs from the one used for the present axion search in its diameter, which was slightly larger (diameter $\phi = 33.2$ mm, with measured TM_{010}

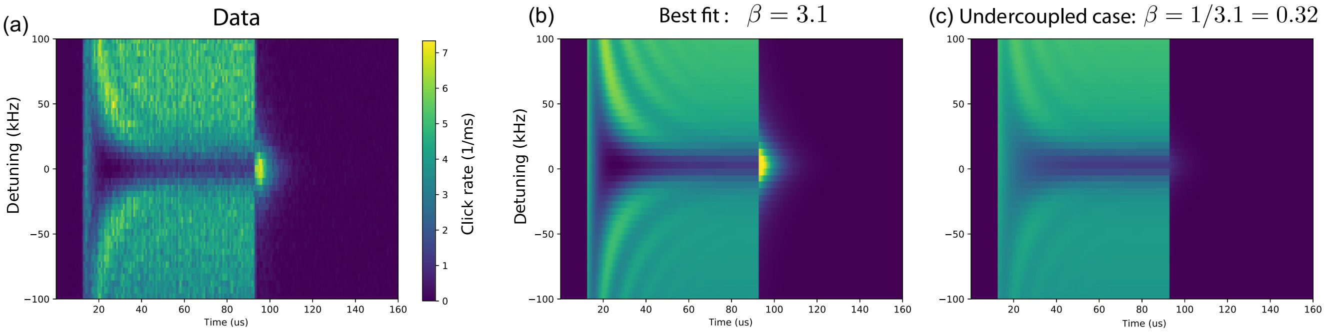

FIG. 12. Time-domain response of the haloscope cavity measured with the SMPD. (a) The click rate of the SMPD is measured in response to a square pulse applied to the haloscope. This measurement is conducted as a function of time and pulse frequency. The SMPD's time resolution is enhanced to 1 μs by reducing the duration of the detection windows. The detection times of the SMPD are sampled to cover the entire time window. (b) Theoretical prediction fitted with $\beta = 3.15$ for the haloscope. All transient features are quantitatively captured by the model lifting the ambiguity toward the overcoupled regime. (c) Theoretical prediction for the same loaded quality factor Q_L but in the undercoupled regime with $\beta = 1/3.15 = 0.32 < 1$. The transient features at the loading and unloading of the haloscope are not reproduced despite that the steady-state absorption is identical to the overcoupled case as expected.

mode frequency $\nu_c = 6.991$ GHz at room temperature). In the measurements shown, the cavity is mounted in a flow cryostat, in which the temperature of the He flow, kept at a pressure of about 600 mbar, is controlled with a thermostat down to 3.5 K. The cavity is inserted in the bore of a solenoid magnet capable of delivering fields exceeding 10 T. Values reported are obtained by doing temperature measurements up to the NbTi critical temperature at zero field and then by cooling down the cavity to the minimum temperature before increasing the magnetic field.

APPENDIX H: AXION SIGNAL POWER

QCD axion models can be probed with cavity haloscope detectors [8,57] in a range from a few hundred megahertz up to about 50 GHz, corresponding to $m_a = h\nu_a = 200$ μeV axion mass. In addition to assuming the existence of axions as exclusive constituent of the galactic dark matter halo [13], detectors rely on their resonant conversion into excitations of a high-quality factor electromagnetic cavity mode, whose electric field is parallel to an applied intense magnetic field. As is the case for the experiment described in this work, the fundamental mode TM_{010} of an empty copper cylinder resonator is typically used, and the signal power P_a is proportional to $(VC_{010}Q_L)$, with $C_{010} = |\int_V dV\mathbf{E}_{010}(\mathbf{x},t)\cdot\mathbf{B}(\mathbf{x})|^2/(\mathbf{B}^2V\int_V dV\mathbf{E}_{010}^2)$, $\mathbf{B}$ the external field, $\mathbf{E}_{010}$ the microwave cavity electric field, V and $Q_L = Q_c/(1+\beta)$, respectively, volume and loaded quality factor of the cavity. β is the coupling strength of a coaxial antenna to the cavity mode. In natural units, the axion power extracted with the antenna at resonance is given by [58]

$$P_a = g_\gamma^2 \frac{\alpha^2}{\pi^2}\frac{\rho_a}{\Lambda^4}\frac{\beta}{1+\beta}2\pi\nu_c B_0^2 V C_{010}\frac{Q_a Q_L}{Q_a + Q_L}, \tag{H1}$$

where α is the fine-structure constant, $\rho_a \simeq 0.45\ \mathrm{GeV/cm^3}$ is the dark matter density in the galactic halo, $\Lambda = 78$ MeV is a parameter linking the axion mass to hadronic physics, and g_γ is the dimensionless axion-photon coupling. The coupling that appears in the axion-photon Lagrangian is $g_{a\gamma\gamma} = (g_\gamma\alpha/\pi\Lambda^2)m_a$. A useful benchmark for experiments is the QCD axion band, delimited by the Kim-Shifman-Vainshtein-Zakharov (KSVZ) [59,60] and Dine-Fischler-Srednicki-Zhitnitsky (DFSZ) [61,62] families of models, with couplings $g_\gamma = -0.97$ and 0.36, respectively. A practical expression for the signal power is

$$P_{a\gamma\gamma} = 0.72\ \mathrm{yW}\left(\frac{g_\gamma}{0.97}\right)^2 \frac{\rho_a}{0.45\ \mathrm{GeV/cm^3}}\left(\frac{B}{2\ \mathrm{T}}\right)^2 \cdot \times \frac{V}{0.11l}\cdot\frac{\nu_c}{7.37\ \mathrm{GHz}}\cdot\frac{Q_L}{225000}\cdot\frac{C_{010}}{0.64}, \tag{H2}$$

in which the parameters of the present experiment are made explicit. The smallness of the signal power, which at DFSZ models is at the yoctowatt (10^{-24} W) level even when state-of-the-art equipment is employed (see Table II), is thus the key methodological challenge for haloscope detectors.

TABLE II. Signal power for benchmark QCD axion models in yoctowatt (yW $= 10^{-24}$ W) and photon rate calculated with Eq. (H1). The right cylinder hybrid surfaced cavity employed in the present experimental apparatus has a fundamental frequency of resonance $\nu_c = 7.37$ GHz (30.48 μeV axion mass), volume $V = 0.1$ l, form factor $C_{010} = 0.64$, and loaded quality factor $Q_L = 2.25\times10^5$). The signal power is also given in the second row for a magnetic field of 12 T, in place of the present superconducting magnet delivering up to a maximum field of 2 T. Coupling coefficient $\beta = 1$ has been assumed. For comparison, a haloscope probing heavier axions ($\nu_c = 10$ GHz corresponds to 41.36 μeV) is also considered, having the same pillbox cavity length (0.135 m).

	B (T)	P_a^{KSVZ} [yW(ph/s)]	P_a^{DFSZ} [yW(ph/s)]
$\nu_c = 7.37$ GHz	2	0.84(0.17)	0.11(0.026)
	12	30.4(6.2)	6.3(0.86)
$\nu_c = 10$ GHz	12	22.39(3.38)	3.11(0.47)

The signal power spectrum is a Maxwell-Boltzmann distribution, with $\Delta\nu_a = \nu_a/Q_a$ width and $Q_a = 10^6$ set by axion velocities dispersion in the standard halo model [13]. Note that, though the resonant enhancement is reduced at critical coupling to the receiver chain ($\beta = 1$) in a cavity haloscope, the optimal coupling maximizes the search speed, and $\beta \sim 2$ or greater is typically chosen.

APPENDIX I: SCAN RATE

Given that the axion mass m_a is unknown, the merit of a cavity haloscope design is typically evaluated using the scan rate df/dt. This parameter quantifies the maximum speed at which a search can be run at sensitivity $g_{a\gamma\gamma} \propto m_a$ and is given by [63]

$$\frac{df}{dt} \approx \frac{g_{a\gamma\gamma}^4}{\Sigma^2}\frac{\rho_a^2}{m_a^2}\frac{B_0^4 C_{010}^2 V^2}{N_{\mathrm{sys}}^2}\left(\frac{\beta}{1+\beta}\right)^2\frac{Q_L Q_a^2}{Q_L + Q_a}, \tag{I1}$$

where $N_{\mathrm{sys}} = k_B T_s$ is the system noise [17] with known noise temperature T_n. For an amplifier at SQL, $k_B T_s = h\nu$; thus, $df/dt \propto \nu^{-4}$ if we fix the cavity length to a value h comparable with the typical length of a commercially available SC solenoid (approximately 25 cm). In fact, $V \propto \nu_c^{-2}$ because in a cylindrical cavity $r = 2.405c/(2\pi\nu_c)$, $m_a \simeq h\nu_c$, and in addition we drop the quality factor frequency dependence $Q_L \propto \nu^{-2/3}$ related to the anomalous skin effect [64], because we consider superconducting cavities. Even though we allow for rather extreme values of cavity aspect ratio $h/r \simeq 10$, with r the cavity radius, the intruder modes density is acceptable in the 5–10 GHz range, where a few different radius resonators could be envisaged to cover the whole range.

APPENDIX J: PHOTON COUNTING VERSUS LINEAR DETECTION

The comparison between linear detection and photon counting was thoroughly analyzed in the foundational study by Lamoureaux *et al.* in Ref. [17]. This analysis is revised and contextualized here, articulated through the lens of experimental parameters, especially focusing on detector efficiency and dark counts. The case where the axion linewidth is smaller than the haloscope linewidth $\Delta\nu_a < \Delta\nu_c$ is considered. In the opposite limit, the analysis holds by substituting the axion linewidth with the haloscope linewidth ($\Delta\nu_a \leftarrow \Delta\nu_c$).

Linear amplifiers are widely utilized for detecting incoherent signals. Consideration is given to an axion signal with power P_a, incoherently emitted across a bandwidth $\Delta\nu_a$ at a frequency ν_a, which is predicted by the axion model to typically have a quality factor $Q_a = \nu_a/\Delta\nu_a \sim 10^6$. The noise generated by the linear receiver over a measurement duration t is expressed as

$$P_{\mathrm{lin}} = h\nu_a(\overline{n}+1)\sqrt{\frac{\Delta\nu_a}{t}}, \tag{J1}$$

where the mean photon number per mode is given by $\bar{n} = [\exp(h\nu_a/k_bT) - 1]^{-1}$.

On the one hand, when k_bT significantly exceeds $h\nu_a$, this noise limit simplifies to the Dicke radiometer formula: $P_{\mathrm{RM}} = k_bT\sqrt{\Delta\nu_a/t}$. On the other hand, the optimal noise power is achievable at zero temperature and defined as the SQL:

$$P_{\mathrm{SQL}} = h\nu_a\sqrt{\Delta\nu_a/t}. \tag{J2}$$

It is noteworthy that, given the incoherent nature of the expected signal, both I and Q quadratures contribute a vacuum noise of $h\nu_a/2$ leading to noise power of $h\nu_a$ as described in Ref. [17]. The detection's signal-to-noise ratio (SNR) is, therefore, capped as follows:

$$\mathrm{SNR}_{\mathrm{SQL}} = \frac{P_a}{h\nu_a}\sqrt{\frac{t}{\Delta\nu_a}}. \tag{J3}$$

In the current setup, we examine a photon detector characterized by an efficiency η and a dark count rate Γ. The signal is obtained by accumulating counts over a period of t, yielding $S = \eta P_a/h\nu_a t + \Gamma t$. Given its Poisson distribution, the variance associated with this signal is $\delta S^2 = \eta P_a/h\nu_a t + \Gamma t$. The SNR, therefore, reads

$$\mathrm{SNR}_{\mathrm{PC}} = \frac{\eta P_a t/h\nu_a}{\sqrt{\Gamma_{\mathrm{dc}}t + \eta P_a t/h\nu_a}} = \frac{\eta P_a}{h\nu_a}\frac{\sqrt{t}}{\sqrt{\Gamma_{\mathrm{dc}} + \eta P_a/h\nu_a}}. \tag{J4}$$

In situations where signal contribution $\eta P_a/h\nu_a$ is negligible compared to the dark count Γ_{dc}, the noise due to signal shot can be disregarded, leading to the following SNR expression:

$$\mathrm{SNR}_{\mathrm{PC}} \approx \frac{\eta P_a}{h\nu_a}\sqrt{\frac{t}{\Gamma_{\mathrm{dc}}}}. \tag{J5}$$

The dark count rate can be breakdown in two main contributions $\Gamma_{\mathrm{dc}} = \Gamma_{\mathrm{th}} + \Gamma_{\mathrm{int}}$, where $\Gamma_{\mathrm{th}} = \eta\Delta\nu_{\mathrm{det}}n_{\mathrm{th}}$ is the background thermal fluctuation integrated over the detector bandwidth $\Delta\nu_{\mathrm{det}}$ and where Γ_{int} is the intrinsic detector dark count due to technical counts due to, for instance, errors in the qubit readout or out-of-equilibrium excitation of the qubit. In the limit where the dark count is dominated by thermal background contribution ($\Gamma_{\mathrm{int}} \ll \eta\Delta\nu_{\mathrm{det}}n_{\mathrm{th}}$), the SNR reads

$$\mathrm{SNR}^{\mathrm{th}}_{\mathrm{PC}} \approx \frac{P_a}{h\nu_a}\sqrt{\frac{\eta t}{\Delta\nu_{\mathrm{det}}n_{\mathrm{th}}}}. \tag{J6}$$

Note that the SMPD used in this experiment operates in this regime [20] where the intrinsic dark count is of the order of $\Gamma_{\mathrm{int}} \sim 10\mathrm{s}^{-1}$ while $\Gamma_{\mathrm{th}} \sim 75\mathrm{s}^{-1}$ corresponding to a microwave temperature of 44 mK where the effective bandwidth of the detector taking into account the Lorentzian linewidth is given by $\Delta\nu_{\mathrm{det}} = \kappa/4 = 2\pi/4 \times 0.7$ MHz.

Our goal is to assess the improvement in measurement speed for achieving a specified SNR. For operations of a linear receiver at the quantum standard limit, the required measurement time is

$$t_{\mathrm{SQL}} = \Delta\nu_a\left(\frac{h\nu_a\mathrm{SNR}}{P_a}\right)^2. \tag{J7}$$

Conversely, for photon counting, the required measurement time is

$$t_{\mathrm{PC}} = \frac{\Gamma_{\mathrm{dc}}}{\eta^2}\left(\frac{h\nu_a\mathrm{SNR}}{P_a}\right)^2. \tag{J8}$$

Hence, the comparative gain in measurement speed or scanning rate in this experiment relative to the quantum standard limit is

$$\mathcal{R} = \frac{t_{\mathrm{SQL}}}{t_{\mathrm{PC}}} = \eta^2\frac{\Delta\nu_a}{\Gamma_{\mathrm{dc}}} \sim 20. \tag{J9}$$

The gain in measurement time can be evaluated in the ideal limit where the dark count is dominated by the background thermal noise and where the detector bandwidth is perfectly matched with the haloscope linewidth ($\Delta\nu_{\mathrm{det}} \approx \Delta\nu_c$); then the gain is given by

$$\mathcal{R}^{\mathrm{th}} = \frac{t_{\mathrm{SQL}}}{t^{\mathrm{th}}_{\mathrm{PC}}} = \eta\frac{\Delta\nu_a}{n_{\mathrm{th}}\Delta\nu_c}. \tag{J10}$$

Crucially, the enhancement in scan rate achievable through photon counting, as compared to linear detection, is not subject to any fundamental limits. In particular, expected advancements in reducing the dark count rate, enhancing efficiency, and achieving stability (thereby negating the need for the differential method) promise to unlock substantially greater improvements in speed.

APPENDIX K: TEMPERATURE ESTIMATION OF THE ELECTROMAGNETIC MODES FROM PHOTON COUNTING MEASUREMENT RECORD

The counts measured by the SMPD are related to the temperature of the itinerant microwave modes impinging on the detector. The counts originate from two sources: the detector's intrinsic dark counts, Γ_{int}, and the thermal photons coming from the lines, Γ_{th}. The intrinsic dark counts can be measured by detuning the pump from its four-wave-mixing frequency matching condition such that the detection efficiency vanishes, yielding an average intrinsic dark count rate of $\Gamma_{\mathrm{int}} = 15 \pm 5\mathrm{s}^{-1}$. This includes spurious excitations from the qubit and unwanted heating due to the pump [20]. The contribution of the line to the counts, Γ_{th}, is related to the thermal occupation of the line by

$$\Gamma_{\mathrm{th}} = \Gamma_{\mathrm{detuned}} - \Gamma_{\mathrm{int}} = \eta \frac{\kappa_{\mathrm{det}}}{4} \bar{n}_{\mathrm{th}},$$

where $\bar{n}_{\mathrm{th}} = (\exp(h\nu_c/k_B T) - 1)^{-1}$ is the mean thermal occupancy of the line modes and $\kappa_{\mathrm{det}} = 2\pi \times 0.7$ MHz is the SMPD Lorentzian linewidth. We can, therefore, estimate the line temperature by considering the counts measured when the SMPD is detuned from the haloscope displayed in Fig. 3(c). The mode occupancy of the line reads $\bar{n}_{\mathrm{detuned}} = (1.57 \pm 0.1) \times 10^{-4}$, yielding an average microwave temperature of 39.9 ± 0.6 mK.

Now we turn to the estimation of the noise temperature coming from the loss channel of the haloscope. The haloscope loss channel emits to the line with a transmission coefficient given by $T[\delta\omega] = \{4\beta\kappa_0^2/[\kappa_0^2(1+\beta)^2 + 4\delta\omega^2]\}$ with $\kappa_0/2\pi = f_0/Q_0 = 8.1$ kHz and $\delta\omega$ the angular frequency detuning from the haloscope resonance. The contribution of this loss channel to the total counts can be calculated by integrating the transmission coefficient over frequency [20] considering that the detector efficiency is constant over the haloscope frequency scale:

$$\Gamma_{\mathrm{halo}} = \eta \bar{n}_{\mathrm{th,halo}} \int T[\delta\omega] \frac{d\omega}{2\pi} = \eta \bar{n}_{\mathrm{th,halo}} \frac{\beta}{1+\beta} \kappa_0. \quad (\mathrm{K1})$$

$\Gamma_{\mathrm{halo}} = \Gamma_{\mathrm{tuned}} - \Gamma_{\mathrm{detuned}}$ is measured accurately through the differential measurement as depicted in Fig. 3(d); therefore, we can infer the thermal population associated to the loss channel of the haloscope to be $\bar{n}_{\mathrm{th,halo}} = (1.0 \pm 0.1) \times 10^{-2}$. This translates into a haloscope microwave temperature of (76 ± 2) mK. This temperature is significantly higher than the one of the line which is expected as the haloscope is further away from the mixing chamber and is significantly heated by the attocube stepper employed to tune its frequency. Although this temperature is significantly higher, it still contributes marginally to the overall dark counts as the linewidth of the cavity remains much smaller than the linewidth of the detector.

[1] J. R. Primack, *Triumphs and tribulations of* λCDM*, the double dark theory*, Ann. Phys. (Berlin) **524**, 535 (2012).

[2] G. Bertone and D. Hooper, *History of dark matter*, Rev. Mod. Phys. **90**, 045002 (2018).

[3] G. Bertone, *The moment of truth for wimp dark matter*, Nature (London) **468**, 389 (2010).

[4] J. Liu, X. Chen, and X. Ji, *Current status of direct dark matter detection experiments*, Nat. Phys. **13**, 212 (2017).

[5] D. DeMille, J. M. Doyle, and A. O. Sushkov, *Probing the frontiers of particle physics with tabletop-scale experiments*, Science **357**, 990 (2017).

[6] A. O. Sushkov, *Quantum science and the search for axion dark matter*, PRX Quantum **4**, 020101 (2023).

[7] C. L. Degen, F. Reinhard, and P. Cappellaro, *Quantum sensing*, Rev. Mod. Phys. **89**, 035002 (2017).

[8] P. Sikivie, *Invisible axion search methods*, Rev. Mod. Phys. **93**, 015004 (2021).

[9] F. Chadha-Day, J. Ellis, and D. J. E. Marsh, *Axion dark matter: What is it and why now?*, Sci. Adv. **8**, eabj3618 (2022).

[10] C. Bartram *et al.*, *Search for invisible axion dark matter in the* 3.3 − 4.2 μeV *mass range*, Phys. Rev. Lett. **127**, 261803 (2021).

[11] A. K. Yi *et al.*, *Axion dark matter search around* 4.55 μeV *with Dine-Fischler-Srednicki-Zhitnitskii sensitivity*, Phys. Rev. Lett. **130**, 071002 (2023).

[12] D. Ahn *et al.*, *Biaxially textured* $\mathrm{YBa_2Cu_3O_{7-x}}$ *microwave cavity in a high magnetic field for a dark-matter axion search*, Phys. Rev. Appl. **17**, L061005 (2022).

[13] M. S. Turner, *Cosmic and local mass density of, "invisible" axions*, Phys. Rev. D **33**, 889 (1986).

[14] K. Yamamoto *et al.*, *The Rydberg-atom-cavity axion search*, in *Dark Matter in Astro- and Particle Physics*, edited by H. V. Klapdor-Kleingrothaus (Springer, Berlin, 2001), pp. 638–645.

[15] M. Malnou, D. A. Palken, B. M. Brubaker, L. R. Vale, G. C. Hilton, and K. W. Lehnert, *Squeezed vacuum used to accelerate the search for a weak classical signal*, Phys. Rev. X **9**, 021023 (2019).

[16] K. M. Backes *et al.*, *A quantum enhanced search for dark matter axions*, Nature (London) **590**, 238 (2021).

[17] S. K. Lamoreaux, K. A. van Bibber, K. W. Lehnert, and G. Carosi, *Analysis of single-photon and linear amplifier detectors for microwave cavity dark matter axion searches*, Phys. Rev. D **88**, 035020 (2013).

[18] S. Diamond *et al.*, *Distinguishing parity-switching mechanisms in a superconducting qubit*, PRX Quantum **3**, 040304 (2022).

[19] T. Connolly, P. D. Kurilovich, S. Diamond, H. Nho, C. G. L. Bottcher, L. I. Glazman, V. Fatemi, and M. H. Devoret, *Coexistence of nonequilibrium density and equilibrium energy distribution of quasiparticles in a superconducting qubit*, Phys. Rev. Lett. **132**, 217001 (2024).

[20] L. Balembois *et al.*, *Cyclically operated microwave single-photon counter with sensitivity of* 10^{-22} W/$\sqrt{\mathrm{Hz}}$, Phys. Rev. Appl. **21**, 014043 (2024).

[21] A. V. Dixit, S. Chakram, K. He, A. Agrawal, R. K. Naik, D. I. Schuster, and A. Chou, *Searching for dark matter with a superconducting qubit*, Phys. Rev. Lett. **126**, 141302 (2021).

[22] D. Alesini *et al.*, *Galactic axions search with a superconducting resonant cavity*, Phys. Rev. D **99**, 101101(R) (2019).

[23] R. Lescanne, S. Deleglise, E. Albertinale, U. Reglade, T. Capelle, E. Ivanov, T. Jacqmin, Z. Leghtas, and E. Flurin, *Irreversible qubit-photon coupling for the detection of itinerant microwave photons*, Phys. Rev. X **10**, 021038 (2020).

[24] J. Gambetta, A. Blais, D. I. Schuster, A. Wallraff, L. Frunzio, J. Majer, M. H. Devoret, S. M. Girvin, and R. J. Schoelkopf, *Qubit-photon interactions in a cavity: Measurement-induced dephasing and number splitting*, Phys. Rev. A **74**, 042318 (2006).

[25] E. Albertinale *et al.*, *Detecting spins by their fluorescence with a microwave photon counter*, Nature (London) **600**, 434 (2021).

[26] Z. Wang *et al.*, *Single-electron spin resonance detection by microwave photon counting*, Nature (London) **619**, 276 (2023).

[27] G. Vianello, *The significance of an excess in a counting experiment: Assessing the impact of systematic uncertainties and the case with a Gaussian background*, Astrophys. J. Suppl. Ser. **236**, 17 (2018).

[28] P. V. Klimov *et al.*, *Fluctuations of energy-relaxation times in superconducting qubits*, Phys. Rev. Lett. **121**, 090502 (2018).

[29] W. U. Wuensch *et al.*, *Results of a laboratory search for cosmic axions and other weakly coupled light particles*, Phys. Rev. D **40**, 3153 (1989).

[30] J. Jeong, S. W. Youn, S. Bae, J. Kim, T. Seong, J. E. Kim, and Y. K. Semertzidis, *Search for invisible axion dark matter with a multiple-cell haloscope*, Phys. Rev. Lett. **125**, 221302 (2020).

[31] Y. Lee, B. Yang, H. Yoon, M. Ahn, H. Park, B. Min, D. L. Kim, and J. Yoo, *Searching for invisible axion dark matter with an 18 t magnet haloscope*, Phys. Rev. Lett. **128**, 241805 (2022).

[32] B. Yang, H. Yoon, M. Ahn, Y. Lee, and J. Yoo, *Extended axion dark matter search using the CAPP18t haloscope*, Phys. Rev. Lett. **131**, 081801 (2023).

[33] Y. Kim *et al.*, *Experimental search for invisible dark matter axions around* 22 μeV, Phys. Rev. Lett. **133**, 051802 (2024).

[34] B. M. Brubaker *et al.*, *First results from a microwave cavity axion search at* 24 μeV, Phys. Rev. Lett. **118**, 061302 (2017).

[35] L. Zhong *et al.*, *Results from phase 1 of the haystac microwave cavity axion experiment*, Phys. Rev. D **97**, 092001 (2018).

[36] HAYSTAC Collaboration, *Dark matter axion search with haystac phase II*, arXiv:2409.08998.

[37] M. J. Jewell *et al.*, *New results from haystac's phase II operation with a squeezed state receiver*, Phys. Rev. D **107**, 072007 (2023).

[38] H. Chang *et al.*, *First results from the Taiwan axion search experiment with a haloscope at* 19.6 μeV, Phys. Rev. Lett. **129**, 111802 (2022).

[39] C. M. Adair *et al.*, *Search for dark matter axions with CAST-CAPP*, Nat. Commun. **13**, 6180 (2022).

[40] C. Boutan *et al.*, *Piezoelectrically tuned multimode cavity search for axion dark matter*, Phys. Rev. Lett. **121**, 261302 (2018).

[41] A. Quiskamp, B. T. McAllister, P. Altin, E. N. Ivanov, M. Goryachev, and M. E. Tobar, *Exclusion of axionlike-particle cogenesis dark matter in a mass window above* 100 μeV, Phys. Rev. Lett. **132**, 031601 (2024).

[42] A. P. Quiskamp *et al.*, *Near-quantum limited axion dark matter search with the organ experiment around* 26 μeV, arXiv:2407.18586.

[43] A. Quiskamp *et al.*, *Direct search for dark matter axions excluding alp cogenesis in the 63- to* 67-μeV *range with the organ experiment*, Sci. Adv. **8**, eabq3765 (2022).

[44] T. Grenet *et al.*, *The Grenoble Axion Haloscope platform (GrAHal): Development plan and first results*, https://hal.science/hal-03419781.

[45] A. Álvarez Melcón *et al.*, *First results of the CAST-RADES haloscope search for axions at* 34.67 μeV, J. High Energy Phys. 10 (2021) 075.

[46] D. Alesini *et al.*, *Search for invisible axion dark matter of mass* $\mathrm{m}_a = 43$ μeV *with the QUAX-aγ experiment*, Phys. Rev. D **103**, 102004 (2021).

[47] D. Alesini *et al.*, *Search for galactic axions with a high-q dielectric cavity*, Phys. Rev. D **106**, 052007 (2022).

[48] R. Di Vora *et al.*, *Search for galactic axions with a traveling wave parametric amplifier*, Phys. Rev. D **108**, 062005 (2023).

[49] A. Rettaroli *et al.*, *Search for axion dark matter with the QUAX-LNF tunable haloscope*, Phys. Rev. D **110**, 022008 (2024).

[50] B. A. dos Santos Garcia *et al.*, *First search for axion dark matter with a MADMAX prototype*, arXiv:2409.11777.

[51] L. Di Luzio, F. Mescia, and E. Nardi, *Redefining the axion window*, Phys. Rev. Lett. **118**, 031801 (2017).

[52] L. Di Luzio, M. Giannotti, E. Nardi, and L. Visinelli, *The landscape of QCD axion models*, Phys. Rep. **870**, 1 (2020).

[53] C. O'Hare, *cajohare/axionlimits: Axionlimits*, https://cajohare.github.io/AxionLimits/.

[54] J.-H. Yeh, J. LeFebvre, S. Premaratne, F. C. Wellstood, and B. S. Palmer, *Microwave attenuators for use with quantum devices below 100 mK*, J. Appl. Phys. **121**, 224501 (2017).

[55] Z. Wang, S. Shankar, Z. K. Minev, P. Campagne-Ibarcq, A. Narla, and M. H. Devoret, *Cavity attenuators for superconducting qubits*, Phys. Rev. Appl. **11**, 014031 (2019).

[56] N. Roch, E. Flurin, F. Nguyen, P. Morfin, P. Campagne-Ibarcq, M. H. Devoret, and B. Huard, *Widely tunable, nondegenerate three-wave mixing microwave device operating near the quantum limit*, Phys. Rev. Lett. **108**, 147701 (2012).

[57] Y. K. Semertzidis and S. Youn, *Axion dark matter: How to see it?*, Sci. Adv. **8**, eabm9928 (2022).

[58] B. M. Brubaker *et al.*, *First results from a microwave cavity axion search at* 24 μeV, Phys. Rev. Lett. **118**, 061302 (2017).

[59] J. E. Kim, *Weak-interaction singlet and strong CP invariance*, Phys. Rev. Lett. **43**, 103 (1979).

[60] M. Shifman, A. Vainshtein, and V. Zakharov, *Can confinement ensure natural CP invariance of strong interactions?*, Nucl. Phys. **B166**, 493 (1980).

[61] M. Dine, W. Fischler, and M. Srednicki, *A simple solution to the strong CP problem with a harmless axion*, Phys. Lett. B **104**, 199 (1981).

[62] A. R. Zhitnitsky, *Possible suppression of axion-hadron interactions*, Sov. J. Nucl. Phys. **31**, 260 (1980).

[63] D. Kim, J. Jeong, S. Youn, Y. Kim, and Y. K. Semertzidis, *Revisiting the detection rate for axion haloscopes*, J. Cosmol. Astropart. Phys. 03 (2020) 066.

[64] A. B. Pippard and W. L. Bragg, *The surface impedance of superconductors and normal metals at high frequencies II. The anomalous skin effect in normal metals*, Proc. R. Soc A **191**, 385 (1947).